50th AIAA Aerospace Sciences Meeting including the New Horizons Forum and Aerospace Exposition
09 - 12 January 2012, Nashville, Tennessee

AIAA 2012-0656

LIDAR Wind Speed Measurements of Evolving Wind Fields *†

Eric Simley‡ Lucy Y. Pao § Neil Kelley ¶ Bonnie Jonkman ‖ Rod Frehlich **

Light Detection and Ranging (LIDAR) systems are able to measure the speed of incoming wind before it interacts with a wind turbine rotor. These preview wind measurements can be used in feedforward control systems designed to reduce turbine loads. However, the degree to which such preview-based control techniques can reduce loads by reacting to turbulence depends on how accurately the incoming wind field can be measured. Past studies have assumed Taylor's frozen turbulence hypothesis, which implies that turbulence remains unchanged as it advects downwind at the mean wind speed. With Taylor's hypothesis applied, the only source of wind speed measurement error is distortion caused by the LIDAR. This study introduces wind evolution, characterized by the longitudinal coherence of the wind, to LIDAR measurement simulations to create a more realistic measurement model. A simple model of wind evolution is applied to a frozen wind field used in previous studies to investigate the effects of varying the intensity of wind evolution. Simulation results show the combined effects of LIDAR errors and wind evolution for realistic turbine-mounted LIDAR measurement scenarios.

Nomenclature

a	decay parameter for exponential coherence
a_l	decrement parameter for transverse coherence ($l \in \{u, v, w\}$)
b_l	offset parameter for transverse coherence ($l \in \{u, v, w\}$)
D	longitudinal distance between two points or measurement preview distance
F	focal distance
f	frequency (Hz)
θ	LIDAR measurement angle off of longitudinal direction
k	wind velocity wavenumber (m^{-1})
λ	wavelength (m)
R	range along LIDAR beam
r	scan radius for spinning LIDAR scenario
$r_{i,j}$	distance between two points in the yz plane
U	mean wind speed (m/s)
$\bar{u}_{i,j}$	average mean wind speed between two points in the yz plane
ψ	azimuth angle in the rotor plane
$\gamma^2_{xy}(f)$	Coherence between signals x and y

*This work was supported in part by the US National Renewable Energy Laboratory. Additional industrial support is also greatly appreciated.

†Employees of the Midwest Research Institute under Contract No. DE-AC36-99GO10337 with the U.S. Dept. of Energy have authored this work. The United States Government retains, and the publisher, by accepting the article for publication, acknowledges that the United States Government retains a non-exclusive, paid-up, irrevocable, worldwide license to publish or reproduce the published form of this work, or allow others to do so, for the United States Government purposes.

‡Doctoral Candidate, Dept. of Electrical, Computer, and Energy Engineering, University of Colorado, Boulder, CO, Student Member AIAA.

§Richard and Joy Dorf Professor, Dept. of Electrical, Computer, and Energy Engineering, University of Colorado, Boulder, CO, Member AIAA.

¶Principal Scientist, National Wind Technology Center, NREL, Golden, CO 80401.

‖Senior Scientist, National Wind Technology Center, NREL, Golden, CO 80401.

**Senior Research Associate, Cooperative Institute for Research in Environmental Sciences, Boulder, CO 80309.

Copyright © 2012 by the American Institute of Aeronautics and Astronautics, Inc. Under the copyright claimed herein, the U.S. Government has a royalty-free license to exercise all rights for Go

$S_{xx}(f)$ Power spectral density (PSD) of signal x
$S_{xy}(f)$ Cross-power spectral density (CPSD) between signals x and y

I. Introduction

Wind speed measurements in front of a wind turbine can be used as part of feedforward or preview-based controllers to help mitigate structural loads caused by turbulent wind conditions. Prior analyses have shown that reductions in turbine loads can be achieved with knowledge of the incoming wind field.[1–3] A block diagram of such a control strategy is shown in Fig. 1. Upstream wind is measured, providing an estimate of the wind speeds that will eventually reach the turbine after a delay time of D/U, where D is the preview distance between the rotor and the measurement location and U is the mean wind speed. In reality, the turbulent structures in the wind will evolve between the time they are measured and when they reach the turbine, causing errors in the preview wind measurements.[4] Since wind evolution is due to physical properties of the atmosphere that can only be estimated, it is represented as part of the "plant" of the control system architecture. Wind evolution and LIDAR blocks are shown as part of the control system because their known and estimated effects will have an impact on how the controller is designed.

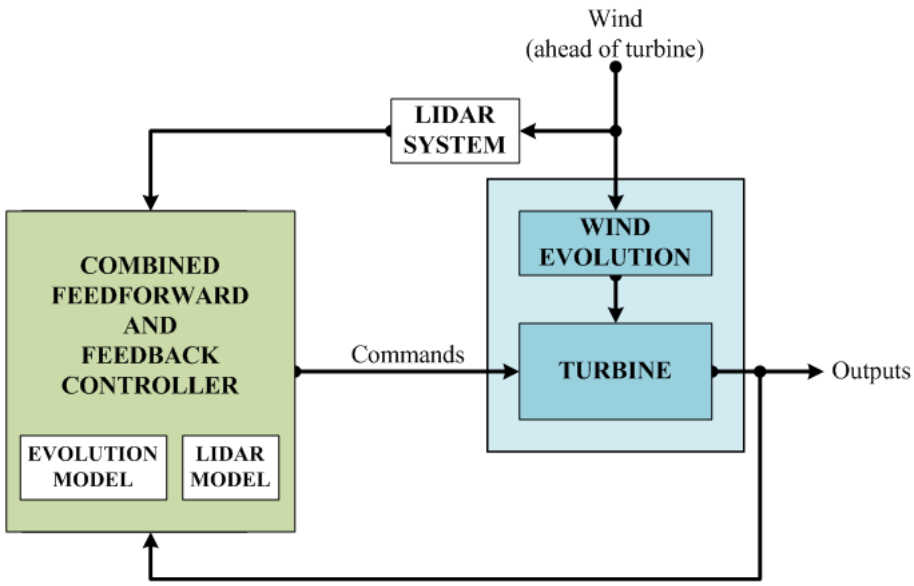

Figure 1. A block diagram illustrating how LIDAR is used in a preview based combined feedforward/feedback control scenario. The wind evolution block represents the coherence loss between wind at the measurement location and the wind encountered by the rotor after a delay time of D/U. The distance D is the distance upwind of the rotor where the measurement is taken and U is the mean wind speed.

Previous work combining preview measurement-based control systems and LIDAR models[5,6] assumed the validity of Taylor's frozen turbulence hypothesis, which claims that turbulent eddies remain unchanged while advecting with the average wind velocity. In this paper we combine our existing model[7] of LIDAR measurements with a model of wind evolution to study the degree to which wind inflow can be accurately measured and the scenarios that provide the best measurements.

In addition to wind evolution, another source of wind distortion exists, which is caused by the induction zone of the turbine. The induction zone has the effect of slowing down the mean velocity of the wind near the rotor and altering the turbulence characteristics.[8] The important topic of wind inflow distortion is an area of future research and is not addressed in this paper, where we consider only the effects of freestream wind evolution.

Wind evolution is described here by the coherence between wind speeds at two points separated longitudinally (in the mean wind direction) in the flow. Taylor's hypothesis in frozen wind fields is equivalent to assuming a coherence function of 1 at all frequencies for all purely longitudinal separations. Wind speeds

at two locations separated longitudinally would simply be delayed versions of each other, with a delay time of D/U. Introducing wind evolution to a frozen wind field is equivalent to applying a coherence function to the wind at locations separated longitudinally in addition to the transverse coherence (perpendicular to the mean wind direction) already provided by most wind models.

In this paper we investigate LIDAR measurement quality for realistic LIDAR scanning scenarios in evolving wind fields. A frozen, or non-evolving, wind field generated using the National Renewable Energy Laboratory's (NREL's) TurbSim[9] code is coupled with a simple longitudinal coherence model to create an evolving wind field. The longitudinal coherence model can be adjusted to simulate varying degrees of wind evolution. Using this wind field, we analyze LIDAR measurement quality for different measurement geometries by calculating the coherence between the measured wind and the evolved wind that reaches the turbine rotor plane. Instead of directly simulating LIDAR measurements in four-dimensional wind fields, we use the spectra of the wind and the transverse and longitudinal coherence functions to calculate the overall measurement coherence.

A previous study by the authors[7] examined the effects of LIDAR on measurement error for realistic scenarios involving the National Renewable Energy Laboratory's (NREL's) 5-MW wind turbine model[10] with frozen wind fields generated by TurbSim, including the wind field that is coupled with a model of wind evolution in this paper. Emphasis was placed on a hub-mounted LIDAR scenario where the LIDAR scanned a circle of wind in front of the rotor. We found that for a continuous-wave (CW) LIDAR model, there is an optimal preview distance for each scan radius where the minimum measurement error is achieved (see Fig. 2 for a depiction of the preview distance D and scan radius r). For a scan radius of 75% blade span (47.25 m for the 5-MW model), which is a radius of particular interest due to maximum power capture,[1–3] optimal preview distances are near 150 meters. In this paper, we provide more realistic acheivable measurement errors and optimal preview distances for the same measurement scenarios, with wind evolution incorporated.

This paper is organized as follows. In Section II, we present the principal equation used in our CW LIDAR model, called the "range weighting function," as well as the process through which the longitudinal component of wind speed is estimated from a line-of-sight measurement. The ways that range weighting and measurement geometry cause measurement errors are discussed here. Results from a realistic hub-mounted LIDAR measurement simulation are provided in Section II-C, revealing the performance that can be expected in the absence of wind evolution. An introduction to coherence and an explanation of how a wind field can be described using coherence functions is provided in Section III. In Section IV, we discuss the frozen wind field generated using the Great Plains-Low Level Jet model in TurbSim. The simple longitudinal coherence model used to introduce wind evolution to the frozen TurbSim wind field is described next. In Section V, we derive the calculations used to determine the coherence between a LIDAR wind speed measurement and the wind that actually reaches the turbine rotor. Section VI includes results for measurement coherence using the calculations derived in Section V as functions of scan radius and preview distance. Finally, Section VII concludes the paper with a discussion of the coherence model and simulation results, and areas of future research.

II. LIDAR Measurements

The analysis of wind speed measurement examined here uses the coordinate system shown in Fig. 2. The ground referenced x, y, and z axes are defined such that -z is pointing in the direction of gravity and x is nominally pointing in the downwind direction. The wind speed vector is defined by u, v, and w components, where u is the streamwise component. Nominally, the u, v, and w axes are aligned with the x, y, and z axes, respectively, since the mean wind direction of the wind fields is in the x direction. The 5-MW wind turbine model, which our measurement geometry is based on, has a hub height of 90 meters and a rotor diameter of 126 meters.

The LIDAR measurement model we have created introduces two imperfections to wind speed measurements in frozen wind fields. Range weighting is the effect inherent to CW and pulsed LIDAR that acts as a spatial filter along the laser beam causing wind speeds at locations other than the focal distance to contribute to the measured value. The other primary source of error in wind speed measurements is due to estimating the u component of the wind velocity vector given a single line-of-sight measurement. This estimation problem is sometimes called the "cyclops dilemma." Control systems utilizing preview wind speed measurements primarily focus on the component of the wind that is perpendicular to the rotor plane, nominally the u component. We are assuming that the rotor plane is always perpendicular to the x axis.

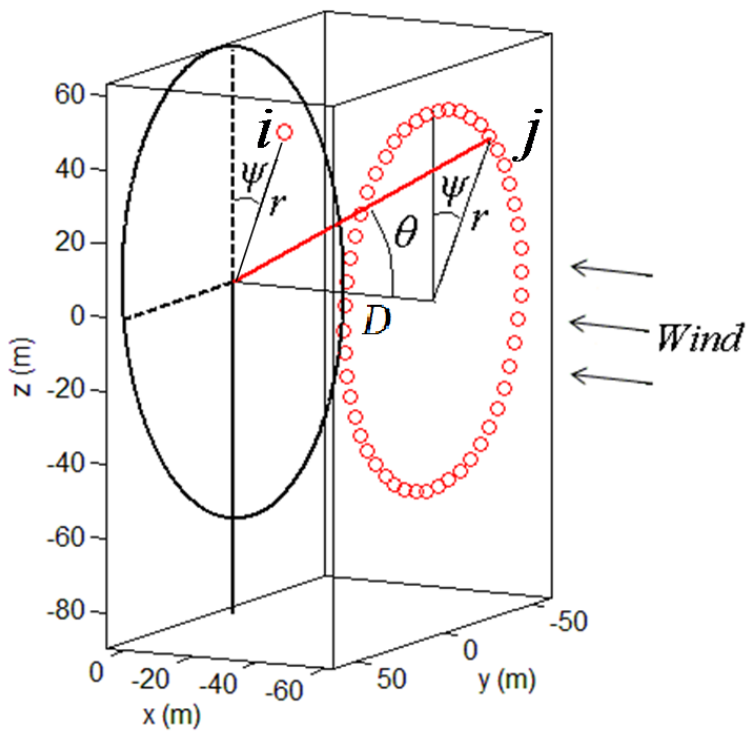

Figure 2. Coordinate system and measurement variables used. The LIDAR is assumed to be mounted in the wind turbine hub at $(x_h, y_h, z_h) = (0, 0, 0)$. The variable D represents the distance upwind, or in the longitudinal direction between the LIDAR and the measurement point. θ is the angle off of the longitudinal wind direction that the LIDAR is pointing. r is the radial distance from the longitudinal direction upwind of the LIDAR to the measurement point in the yz plane. In this figure, r is the radius of the scan pattern of a LIDAR measuring a circle upwind of the rotor. The dots represent where measurements would be taken for a LIDAR with a 50 Hz sampling rate scanning at 60 RPM. This scenario will be discussed throughout the paper. ψ is the azimuth angle of a LIDAR measurement in the yz plane. Point j indicates where a wind speed measurement is taken to estimate the wind that reaches point i after a delay time of D/U.

Therefore, our LIDAR measurements estimate the component of wind aligned with the x axis, which will be treated as equivalent to the u component for the rest of the paper. When the LIDAR is staring in the x direction, there will be no geometrical measurement errors because the v and w components do not contribute to the detected radial velocity. If the laser is instead pointing in a direction other than parallel to the x axis, unknown v and w components contribute to the measurement and an estimate of the u component must be formed. This latter source of error is referred to as "directional bias" in this paper.

A. Range Weighting

Continuous-wave LIDAR determines the line-of-sight wind speed at a specific location by focusing the laser beam at that position in space. Rather than only detecting the wind speed at the intended point, a focal distance F away from the LIDAR, wind speed values along the entire laser beam are averaged according to what is called the "range weighting function," $W(F, R)$, to yield the detected value. The general effect of range weighting is the low-pass filtering of the true wind speed. As focal length increases, more high frequency wind information is lost in the measurement. The line-of-sight wind speed measurement due to range weighting at a focal distance F is given by

$$u'_{LOS}(F) = \int_{-\infty}^{\infty} u_{LOS}(R) W(F, R) dR \tag{1}$$

where $u_{LOS}(R)$ is the line-of-sight velocity at a range R along the laser beam.[11] The range weighting function for a focal distance F is given by

$$W(F,R) = \frac{K_N}{R^2 + (1 - \frac{R}{F})^2 R_R^2} \tag{2}$$

where R_R is the Rayleigh range and K_N is a normalizing constant so that the entire range weighting function integrates to 1. For the commercially available ZephIR Doppler LIDAR system modeled here,[12] R_R is approximately 1,570 meters.

The other leading technology for LIDAR wind speed measurements is pulsed LIDAR. Although pulsed LIDAR systems do not rely on focusing a laser at the range of interest as CW systems do, their spatial averaging can be similarly described by a range weighting function. Pulsed LIDARs emit a laser pulse and integrate the backscattered light as the pulse travels through several "range gates." One drawback to using pulsed technology is that more time is required to integrate enough photons to provide a useful velocity estimate. In the remaining sections of this paper, we focus on CW LIDAR for the measurement analyses.

Figure 3 (a) shows the normalized range weighting functions for the CW model at several focal distances and the fixed weighting function for a pulsed model based on the Leosphere Windcube.[12] A previous analysis[7] has shown that the pulsed LIDAR causes roughly the same amount of measurement error as the CW LIDAR focused at 135 meters. The corresponding frequency responses of the weighting functions in terms of wavenumber k are shown in Fig. 3 (b) where the low-pass filter behavior can be seen.

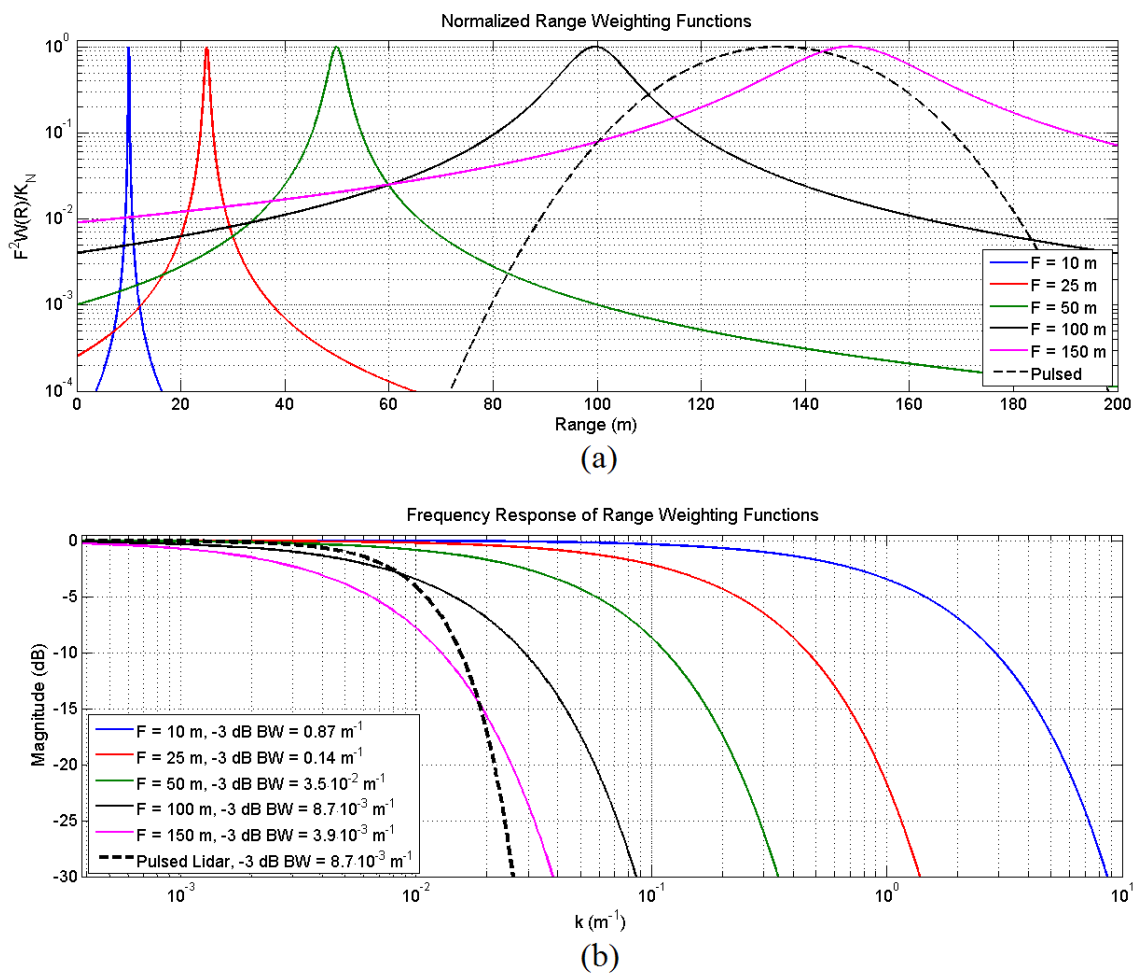

Figure 3. (a) Normalized range weighting functions, $W(F,R)$, for the ZephIR continuous-wave LIDAR at a variety of focal distances, F, and the fixed range weighting function for the Windcube pulsed LIDAR. (b) Frequency responses of the normalized range weighting filters for a variety of focal distances along with the -3 dB bandwidths of the filters.

B. Directional Bias

Since a single LIDAR measurement only provides a line-of-sight velocity, an estimate of the u component of the wind is formed by assuming $v = w = 0$ because ideally $u \gg v, w$. The detected radial velocity when the LIDAR is aimed at an angle θ off of the x direction is given by[7]

$$u_{LOS} = \sqrt{u^2 + v^2 + w^2} \cos\phi \tag{3}$$

where ϕ is the angle between the wind vector and the LIDAR direction. Under the assumption that $v = w = 0$ ($\phi = \theta$), the estimate of u is

$$\hat{u} = \frac{u_{LOS}}{\cos\theta}. \tag{4}$$

When the LIDAR is pointing nearly along the x direction, θ is small and errors due to directional bias are low since the measured radial velocity will be dominated by the u component of wind speed. As θ increases, the radial velocity measured by the LIDAR will contain more contributions from the v and w components, causing higher error. An analysis of directional bias errors[7] has shown that for a variable u velocity and a varying transverse wind speed component with magnitude $\sqrt{v^2 + w^2}$ and uniformly distributed random direction in the yz plane, the RMS measurement error is

$$\sigma_{err} = \frac{\alpha_{RMS} \tan\theta}{\sqrt{2}} \tag{5}$$

where α_{RMS} is the RMS value of the transverse wind speed magnitude, or $\sqrt{\overline{v^2 + w^2}}$.

C. LIDAR Performance in Frozen Wind Fields

Any u component estimate based on a LIDAR measurement in a frozen wind field will contain errors from both range weighting and directional bias as long as the measurement angle is non-zero. A previous study[7] examined measurement errors for a hub-mounted LIDAR scanning a circle of wind with radius r in front of the turbine as a function of preview distance D (see Fig. 2). This scenario is motivated by the need for only one LIDAR, simplicity of implementation, and successful field testing.[13] For short preview distances D, the measurement angles θ tend to be very large, causing large directional bias errors proportional to $\tan\theta$, as shown in equation 5. However, for large preview distances with smaller values of θ, range weighting from a CW LIDAR causes errors to be high. In the absence of wind evolution, it was found that for a CW LIDAR, there is an optimal preview distance for each scan radius r where the combined effects from range weighting and directional bias lead to a minimum achievable RMS error.

A summary of the error vs. preview distance study is provided in Fig. 4 for $r = 50\%$, 75%, and 100% blade span for the 5-MW model turbine (31.5, 47.25, and 63 meters, respectively). Results are shown for the CW and pulsed models using an unstable Great Plains-Low Level Jet wind condition, described in Section IV in Table 1. For CW LIDAR, the minimum-error preview distance is roughly 115 meters for $r = 50\%$ blade span, just under 150 meters for $r = 75\%$ blade span, and over 200 meters for $r = 100\%$ blade span. Note that for pulsed LIDAR there is no minimum-error preview distance in the absence of wind evolution because the range weighting function remains the same as preview distance increases. A goal of the research presented in this paper is to provide more accurate error vs. preview distance curves with the effects of wind evolution, described by longitudinal coherence loss, discussed in the next section, introduced.

III. Coherence in Wind Fields

A. Coherence

The degree to which wind speeds at any two points in a wind field are correlated is given by a coherence function. Coherence will vary depending on the spatial separation of the two points of interest. Wind fields used in a previous study of LIDAR performance[7] included coherence between wind speeds separated in the transverse direction, or the direction perpendicular to the wind direction. However, using Taylor's hypothesis, wind speeds at points separated in the longitudinal, or mean wind direction are always perfectly correlated. In this section, we describe the coherence between wind speeds at any two points in a wind field with wind evolution included. Magnitude-squared coherence, the definition used in this paper is a function

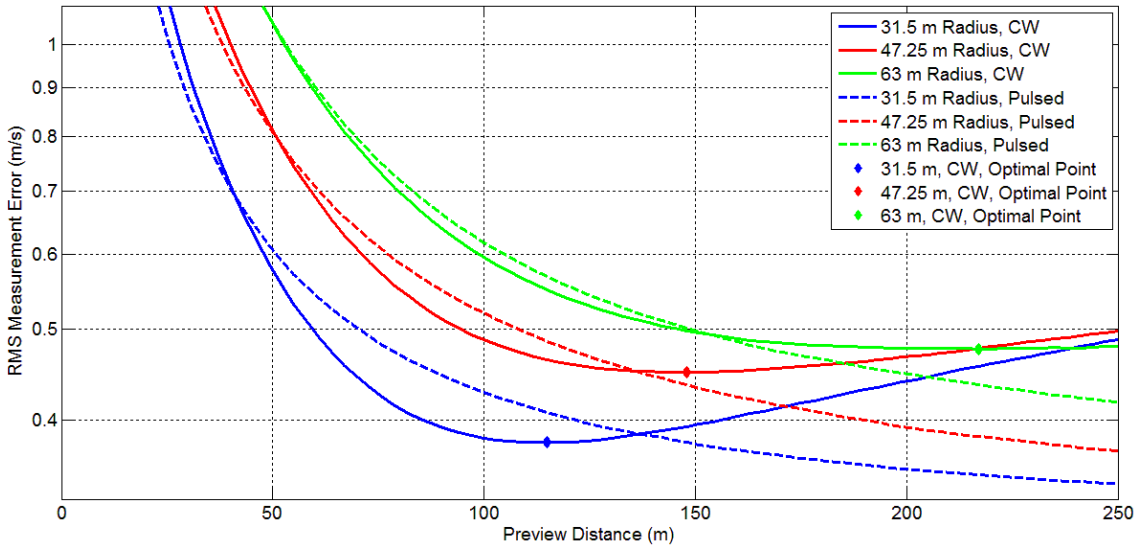

Figure 4. RMS measurement error as a function of preview distance for the 5-MW turbine model in a wind field generated using TurbSim with parameters given in Table 1. Results are shown for CW and Pulsed LIDARs scanning at radii of 50%, 75%, and 100% blade span (blade span for the 5-MW turbine is 63 meters).

of frequency, where a value of 1 indicates that wind is perfectly correlated at the two locations and a value of 0 indicates that wind is completely uncorrelated at the two locations. In addition to magnitude, the phase information for wind at the two locations can be used to assess the degree of wind evolution. Under Taylor's frozen turbulence hypothesis, the coherence magnitude would be 1 for all frequencies and the phase would be $2\pi D/\lambda$ for two points longitudinally separated by a distance D, where λ is the wavelength of the turbulent eddies in the flow at the frequency f given by the relationship $\lambda = U/f$.

Magnitude-squared coherence, often notated as γ^2, is defined as

$$\gamma_{xy}^2 = \frac{|S_{xy}|^2}{S_{xx}S_{yy}} \tag{6}$$

where S_{xy} is the cross-power spectral density (CPSD) between signals x and y and S_{xx} is the power spectral density (PSD) of signal x. CPSD is given by

$$S_{xy} = \mathcal{F}\{R_{xy}(\tau)\} \tag{7}$$

where $\mathcal{F}\{\}$ indicates the Fourier transform, and the cross-correlation function $R_{xy}(\tau)$ is defined as

$$R_{xy}(\tau) = \int_{-\infty}^{\infty} x(t)y^*(t+\tau)dt. \tag{8}$$

The phase associated with coherence is given by

$$\phi_{xy}(f) = \angle(S_{xy}). \tag{9}$$

B. Correlation between Points in a Wind Field

In order to describe the correlation between all points in a wind field with three spatial dimensions, a coherence function must exist for each pair of points. For a wind field with two spatial dimensions, as illustrated in Fig. 5, each wind speed location must be correlated with each other location in the longitudinal, transverse (vertical in this example), and diagonal directions. The wind evolution scenario examined in this paper, described in Section IV, involves introducing wind evolution to a frozen wind field using a simple analytic formula for longitudinal coherence. Transverse coherence functions are already defined for the wind field and longitudinal coherence must be introduced, but there is some ambiguity in the correlation between points separated diagonally, or with some combination of transverse and longitudinal separation.

When introducing wind evolution to a frozen wind field, the diagonal coherence functions must be defined. A range of possibilities exist, but a simple solution is to restrict the diagonal coherence functions to be the product of the coherence resulting from the transverse separation and the coherence resulting from the longitudinal separation. This form of diagonal coherence is illustrated in Fig. 5 and is the coherence that would result if the wind speeds at points x_1, z_1 and x_1, z_2 were correlated independently from the wind speeds at points x_1, z_2 and x_3, z_2. Evaluations of diagonal coherence functions in a stable large eddy simulation (LES) wind field with mean wind speed $U = 7.6$ m/s show that this assumption is very accurate for short longitudinal separations (below ∼30 meters) and is a lower bound on the true diagonal coherence.

For wind fields with three spatial dimensions, nine coherence functions exist to describe the correlation between wind speeds at two different points. Each of the u, v, and w components at one point are correlated with each component at the other point. For the Great Plains-Low Level Jet wind field used in this paper, all of these coherence functions are non-zero, which will be discussed more in Section IV. In general, the correlations between the u components, the v components, and the w components at both points are greater than the "cross" component correlations.

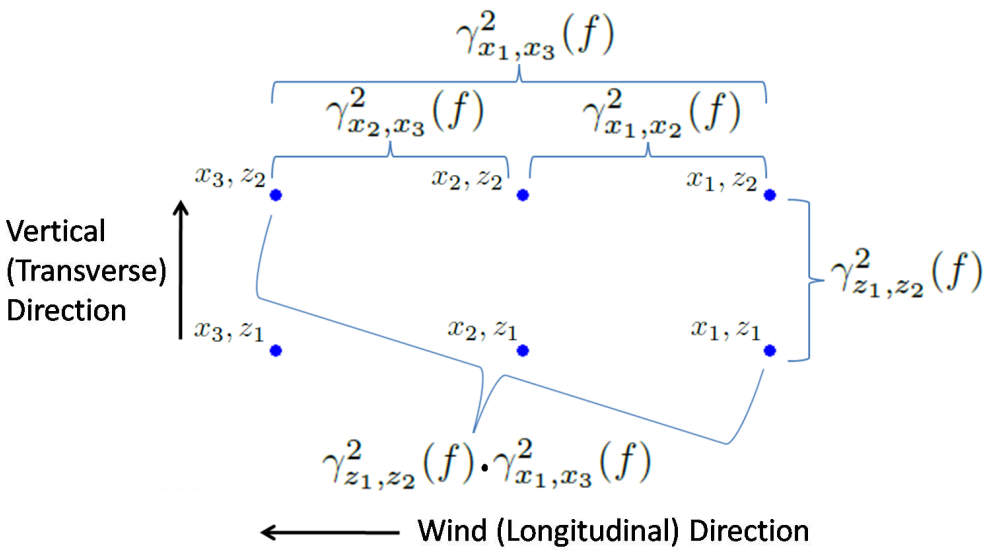

Figure 5. Longitudinal, transverse, and diagonal correlations between wind speed locations in a wind field with two spatial dimensions.

IV. Wind Field and Wind Evolution Model

A wind field characteristic of the U.S. Great Plains region generated by TurbSim is used to demonstrate the addition of wind evolution to a frozen wind field. A simple exponential form of longitudinal coherence is used to create wind evolution in this wind field. By adjusting a decay parameter, the intensity of wind evolution can be varied.

A. The Great Plains-Low Level Jet Wind Field

Wind conditions generated by TurbSim using the Great Plains-Low Level Jet (GP_LLJ) spectral model[9] were used in previous studies[6,7,14] to evaluate LIDAR measurements and controller performance. The wind fields are designed to be used with NREL's 5-MW turbine model with a hub height of 90 m and a rotor radius of 63 m. We have chosen one of these conditions as a wind field to which wind evolution can be introduced. Table 1 summarizes this unstable wind condition at three different heights including hub height and 50 meters below and above hub height.

The spectra of the u, v, and w components of wind speed are shown in Fig. 6 for the heights summarized in Table 1. The spectra are included to illustrate some of the trends that can be seen in the measurement coherence results described in Section VI.

For TurbSim's Great Plains-Low Level Jet spectral model, the transverse coherence at a frequency f

Table 1. A summary of the Great Plains-Low Level Jet wind field used for wind speed measurement analysis with the 5-MW wind turbine model. U indicates the mean streamwise wind speed, Ri_{TL} indicates the turbine layer gradient Richardson number, and α_D indicates the wind shear power law exponent. u^* is the height-dependent friction velocity. Friction velocity is defined as $u^* = \sqrt{\left|\overline{u'w'}\right|}$, where $u' = u - \bar{u}$ and $w' = w - \bar{w}$. TI_U, TI_V, and TI_W are the turbulence intensities of the u, v, and w components of wind speed.

Height (m)	U (m/s)	Ri_{TL}	α_D	u^* (m/s)	TI_U (%)	TI_V (%)	TI_W (%)
40	12.25			0.598	9.2	9.4	7.2
90	13	-0.1	0.077	0.530	6.6	7.1	5.7
140	13.44			0.425	4.6	5.3	4.4

between points i and j in the yz plane is defined as

$$\gamma_{i,j}^2(f,l) = \exp\left(-2a_l\sqrt{\left(\frac{fr_{i,j}}{\bar{u}_{i,j}}\right)^2 + (b_l r_{i,j})^2}\right) \tag{10}$$

where $r_{i,j}$ is the distance between the points, $\bar{u}_{i,j}$ is the average of the wind speeds at the two points, and a_l and b_l are coherence parameters defined for the u, v, and w wind components ($l \in \{u, v, w\}$).[9] The coherence parameters a_l and b_l are based on field measurements and are $a_u = 9.513$, $a_v = 6.291$, and $a_w = 4.535$ and $b_u = 0.384 \cdot 10^{-3}$, $b_v = 0.108 \cdot 10^{-2}$, and $b_w = 0.209 \cdot 10^{-2}$. The u component of transverse coherence given by equation 10 is shown in Fig. 7 (a) for transverse separations of 2, 4, 8, 16, and 32 meters at hub height ($z = 90$ m). This range of distances is indicative of the transverse separations used in calculations of measurement coherence described in the next section.

As mentioned in the previous section, the coherence between the u and v, u and w, as well as v and w components of wind speed is non-zero for the wind field used in this paper. The average Reynolds stress[9] $u'w'$ for this wind field, where $u' = u - \bar{u}$ and $w' = w - \bar{w}$, is -0.281 at hub height, which results in non-zero uw coherence functions. For the u and v components, the average Reynolds stress $u'v'$ is ± 0.277 at hub height, where the sign varies with each 10 minute realization of the wind condition. Furthermore, due to the negative sign of the average $u'w'$ Reynolds stress, the phase of the $u'w'$ coherence function, given by equation 9 is 180°. For consistency, we are treating the sign of the uv correlation as positive. Although the v and w components are correlated as well, the LIDAR measurement scenarios investigated in this paper include either u and v components or u and w components, but not both simultaneously. Therefore, we do not use the vw correlations in any calculations. Figure 7 (b) contains the uw coherence curves for three heights, corresponding to the bottom of the rotor, hub height, and the top of the rotor, as well as the uv coherence function at hub height.

B. Exponential Wind Evolution Model

A model of wind evolution can be formed using a simple exponential model of coherence that is a function of the non-dimensional product between the eddy wavenumber and longitudinal separation, as suggested in Pielke and Panofsky.[15] This model is given by

$$\gamma^2(kD) = e^{-akD} \tag{11}$$

where k is the eddy wavenumber ($k = f/U$), D is the longitudinal separation between points in the wind field, and a is a dimensionless decay parameter. This simple exponential model allows for an easy method of varying the amount of wind evolution by adjusting the decay parameter. Increasing a increases the effects of wind evolution by causing the coherence curve to decay faster with frequency. In Section VI, LIDAR measurement coherence is calculated for the Great Plains-Low Level Jet wind field using this exponential longitudinal coherence function to describe the evolution of the u, v, and w components for a range of decay parameters.

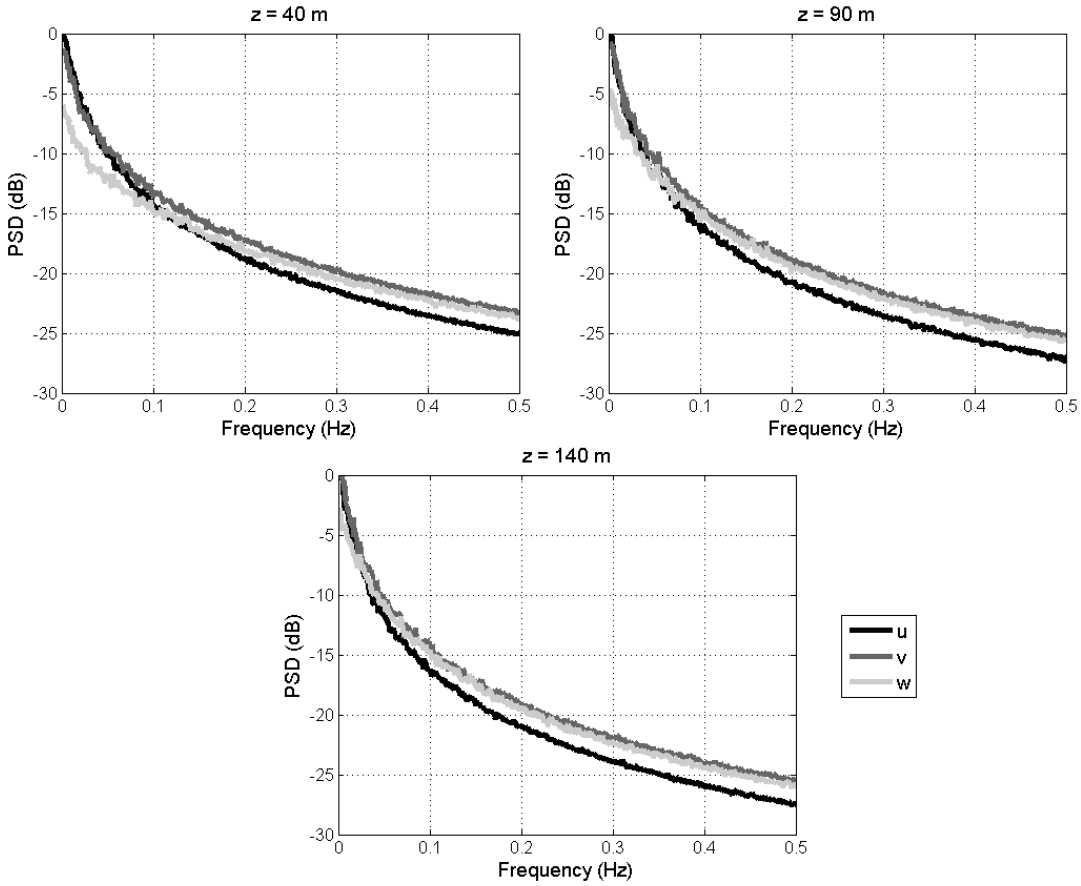

Figure 6. Power spectral densities of wind speed components at heights of 40 m, 90 m, and 140 m for the Great Plains-Low Level Jet wind condition described in Table 1.

V. LIDAR Measurement Coherence

The quality of a wind speed measurement as influenced by evolution can be judged by the coherence between the estimate of the u component of the line-of-sight LIDAR measurement and the true u component that reaches the rotor plane. Referring to Fig. 2, the upwind point at which the LIDAR is focused is called point j, while the point where the evolved wind meets the rotor plane is called point i. Points i and j have the same transverse coordinates but are separated longitudinally by the preview distance D. The coherence between the estimate of the u component at point j and the true u component at point i is written as

$$\gamma^2_{u_i \hat{u}'_j}(f) = \frac{\left| S_{u_i \hat{u}'_j}(f) \right|^2}{S_{u_i u_i}(f)\, S_{\hat{u}'_j \hat{u}'_j}(f)} \tag{12}$$

where $\hat{u}'_j$ represents the estimate of the u component based on the line-of-sight LIDAR measurement. The following derivation of the measurement coherence yields a formula in terms of power spectral densities of the wind and coherence functions for any pair of points in the wind field, which we assume are known quantities based on the wind field description in Section IV. This derivation is based on an analysis given by Schlipf for the simple case where there is neither range weighting nor wind evolution.[16]

If we represent the unit vector in the direction that the LIDAR is pointing as

$$\vec{\ell} = [\ell_x, \ell_y, \ell_z] \tag{13}$$

then based on the coordinate system in Fig. 2, the line-of-sight wind speed measurement is

$$u_{j,LOS} = \ell_x u_j - \ell_y v_j - \ell_z w_j. \tag{14}$$

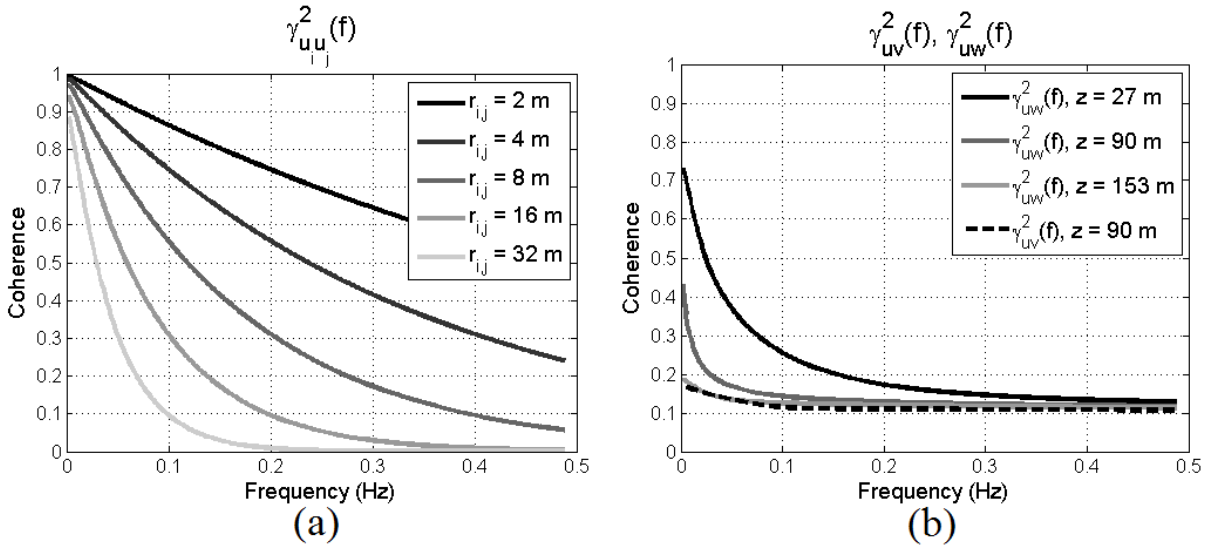

Figure 7. (a) Transverse coherence functions for the u component at a height of $z = 90$ m for transverse separations of 2, 4, 8, 16, and 32 meters. (b) Coherence between the u and w components of wind at $z = 27$ m, 90 m, and 153 m, which correspond to the bottom of the rotor, the hub height, and the top of the rotor, and coherence between the u and v components at $z = 90$ m.

Furthermore, the range weighted line-of-sight measurement is represented as

$$u'_{j,LOS} = \ell_x u'_j - \ell_y v'_j - \ell_z w'_j \tag{15}$$

where the range weighted velocity vector is given by

$$\vec{u}'_j = \int_0^\infty \vec{u}\left(R\vec{\ell}\right) W\left(F,R\right) dR \tag{16}$$

with

$$\vec{u} = [u, v, w]. \tag{17}$$

Based on equations 14 and 15, the estimate of the u component of a line-of-sight point measurement is given by

$$\begin{aligned} \hat{u}_j &= \tfrac{1}{\ell_x} u_{j,LOS} \\ &= u_j - \tfrac{\ell_y}{\ell_x} v_j - \tfrac{\ell_z}{\ell_x} w_j \end{aligned} \tag{18}$$

and the estimate of u for a line-of-sight range weighted measurement is given by

$$\begin{aligned} \hat{u}'_j &= \tfrac{1}{\ell_x} u'_{j,LOS} \\ &= u'_j - \tfrac{\ell_y}{\ell_x} v'_j - \tfrac{\ell_z}{\ell_x} w'_j. \end{aligned} \tag{19}$$

Note that forming an estimate of the u component in equations 18 and 19 by dividing the line-of-sight velocity by ℓ_x is equivalent to dividing the line-of-sight velocity by $\cos\theta$ in equation 4. The measurement angle θ is equivalent to $\arctan\left(\frac{\sqrt{\ell_y^2+\ell_z^2}}{\ell_x}\right)$.

Using equations 13 through 19, the terms $S_{\hat{u}'_j \hat{u}'_j}(f)$ and $S_{u_i \hat{u}'_j}(f)$ from equation 12 can be written in terms of the transverse and longitudinal coherence functions in the wind field and the power spectral density functions of the wind speeds. Letting $\vec{U}(f) = \mathcal{F}\{\vec{u}(t)\}$ and $\{\}^*$ represent the complex conjugate operation, the $S_{\hat{u}'_j \hat{u}'_j}(f)$ term can be expanded as

$$\begin{aligned} S_{\hat{u}'_j \hat{u}'_j}(f) &= \overline{\hat{U}'_j(f)\,\hat{U}'^*_j(f)} \\ &= \overline{\left(\int_0^\infty W(F,\alpha)\,\hat{U}\left(\alpha\vec{\ell},f\right) d\alpha\right)\left(\int_0^\infty W(F,\beta)\,\hat{U}^*\left(\beta\vec{\ell},f\right) d\beta\right)} \\ &= \int_0^\infty \int_0^\infty W(F,\alpha)\,W(F,\beta)\,\overline{\hat{U}\left(\alpha\vec{\ell},f\right)\hat{U}^*\left(\beta\vec{\ell},f\right)} d\alpha\, d\beta \\ &= \int_0^\infty \int_0^\infty W(F,\alpha)\,W(F,\beta)\,S_{\hat{u}_{\alpha\vec{\ell}}\hat{u}_{\beta\vec{\ell}}}(f)\, d\alpha\, d\beta \end{aligned} \tag{20}$$

where $S_{\hat{u}_{\alpha\vec{\ell}}\hat{u}_{\beta\vec{\ell}}}(f)$ is the CPSD between the estimates of the u components at points with distances α and β along the LIDAR beam. For each α, β pair, $S_{\hat{u}_{\alpha\vec{\ell}}\hat{u}_{\beta\vec{\ell}}}(f)$ can be expanded as

$$\begin{aligned} S_{\hat{u}_{\alpha\vec{\ell}}\hat{u}_{\beta\vec{\ell}}}(f) &= \overline{\hat{U}_{\alpha\vec{\ell}}(f)\,\hat{U}^*_{\beta\vec{\ell}}(f)} \\ &= \overline{\left(U_{\alpha\vec{\ell}}(f) - \tfrac{\ell_y}{\ell_x}V_{\alpha\vec{\ell}}(f) - \tfrac{\ell_z}{\ell_x}W_{\alpha\vec{\ell}}(f)\right)\left(U^*_{\beta\vec{\ell}}(f) - \tfrac{\ell_y}{\ell_x}V^*_{\beta\vec{\ell}}(f) - \tfrac{\ell_z}{\ell_x}W^*_{\beta\vec{\ell}}(f)\right)} \\ &= S_{u_{\alpha\vec{\ell}}u_{\beta\vec{\ell}}}(f) + \left(\tfrac{\ell_y}{\ell_x}\right)^2 S_{v_{\alpha\vec{\ell}}v_{\beta\vec{\ell}}}(f) + \left(\tfrac{\ell_z}{\ell_x}\right)^2 S_{w_{\alpha\vec{\ell}}w_{\beta\vec{\ell}}}(f) - \tfrac{\ell_y}{\ell_x}\left(S_{u_{\alpha\vec{\ell}}v_{\beta\vec{\ell}}}(f) + S_{v_{\alpha\vec{\ell}}u_{\beta\vec{\ell}}}(f)\right) \\ &\quad -\tfrac{\ell_z}{\ell_x}\left(S_{u_{\alpha\vec{\ell}}w_{\beta\vec{\ell}}}(f) + S_{w_{\alpha\vec{\ell}}u_{\beta\vec{\ell}}}(f)\right) + \tfrac{\ell_y\ell_z}{\ell_x^2}\left(S_{v_{\alpha\vec{\ell}}w_{\beta\vec{\ell}}}(f) + S_{w_{\alpha\vec{\ell}}v_{\beta\vec{\ell}}}(f)\right). \end{aligned} \tag{21}$$

The measurement scenarios discussed in this paper include azimuth angles of $\psi = 0°$, $\psi = 90°$, $\psi = 180°$, and $\psi = -90°$. As a result, the unit vector in the LIDAR direction either contains $\ell_y = 0$ or $\ell_z = 0$. In this case, equation 21 simplifies to

$$\begin{aligned} S_{\hat{u}_{\alpha\vec{\ell}}\hat{u}_{\beta\vec{\ell}}}(f) &= S_{u_{\alpha\vec{\ell}}u_{\beta\vec{\ell}}}(f) + \left(\tfrac{\ell_y}{\ell_x}\right)^2 S_{v_{\alpha\vec{\ell}}v_{\beta\vec{\ell}}}(f) + \left(\tfrac{\ell_z}{\ell_x}\right)^2 S_{w_{\alpha\vec{\ell}}w_{\beta\vec{\ell}}}(f) - \tfrac{\ell_y}{\ell_x}\left(S_{u_{\alpha\vec{\ell}}v_{\beta\vec{\ell}}}(f) + S_{v_{\alpha\vec{\ell}}u_{\beta\vec{\ell}}}(f)\right) \\ &\quad -\tfrac{\ell_z}{\ell_x}\left(S_{u_{\alpha\vec{\ell}}w_{\beta\vec{\ell}}}(f) + S_{w_{\alpha\vec{\ell}}u_{\beta\vec{\ell}}}(f)\right). \end{aligned} \tag{22}$$

The complex-valued CPSD in equation 22 can be written in terms of its magnitude and phase as

$$S_{\hat{u}_{\alpha\vec{\ell}}\hat{u}_{\beta\vec{\ell}}}(f) = \left|S_{\hat{u}_{\alpha\vec{\ell}}\hat{u}_{\beta\vec{\ell}}}(f)\right| e^{j\phi_{\alpha\vec{\ell}\beta\vec{\ell}}(f)}. \tag{23}$$

Each term in equation 22 has the same phase, which is given by

$$\phi_{\alpha\vec{\ell}\beta\vec{\ell}}(f) = \frac{D_{\alpha\vec{\ell}\beta\vec{\ell}}f}{\overline{U}} \tag{24}$$

where $D_{\alpha\vec{\ell}\beta\vec{\ell}}$ is the longitudinal separation between points at distances α and β along the LIDAR beam. With knowledge of the PSDs of the wind field and the coherence between wind at any two points in the wind field, the magnitudes of the CPSDs can be found by rearranging the formula for coherence in equation 6 as

$$|S_{xy}| = \sqrt{S_{xx}S_{yy}\gamma^2_{xy}}. \tag{25}$$

The calculation of the $S_{u_i\hat{u}'_j}(f)$ term from equation 12 is performed in a similar fashion as the $S_{\hat{u}'_j\hat{u}'_j}(f)$ term. $S_{u_i\hat{u}'_j}(f)$ can be expanded as

$$\begin{aligned} S_{u_i\hat{u}'_j}(f) &= \overline{U_i(f)\,\hat{U}'^*_j(f)} \\ &= \overline{U_i(f)\left(\int_0^\infty W(F,R)\,\hat{U}^*\left(R\vec{\ell},f\right)dR\right)} \\ &= \int_0^\infty W(F,R)\,\overline{U_i(f)\,\hat{U}^*\left(R\vec{\ell},f\right)}dR \\ &= \int_0^\infty W(F,R)\,S_{u_i\hat{u}_{R\vec{\ell}}}(f)\,dR \end{aligned} \tag{26}$$

where $S_{u_i\hat{u}_{R\vec{\ell}}}(f)$ is the CPSD between the u component at point i on the rotor plane and the u estimate based on the line-of-sight point measurement at a distance R along the LIDAR beam. For each distance R, $S_{u_i\hat{u}_{R\vec{\ell}}}(f)$ can be expanded as

$$\begin{aligned} S_{u_i\hat{u}_{R\vec{\ell}}}(f) &= \overline{\hat{U}_i(f)\,\hat{U}^*_{R\vec{\ell}}(f)} \\ &= \overline{U_i(f)\left(U^*_{R\vec{\ell}}(f) - \tfrac{\ell_y}{\ell_x}V^*_{R\vec{\ell}}(f) - \tfrac{\ell_z}{\ell_x}W^*_{R\vec{\ell}}(f)\right)} \\ &= S_{u_iu_{R\vec{\ell}}}(f) - \tfrac{\ell_y}{\ell_x}S_{u_iv_{R\vec{\ell}}}(f) - \tfrac{\ell_z}{\ell_x}S_{u_iw_{R\vec{\ell}}}(f). \end{aligned} \tag{27}$$

Once again, equation 27 can be described by its magnitude and phase as

$$S_{u_i\hat{u}_{R\vec{\ell}}}(f) = \left|S_{u_i\hat{u}_{R\vec{\ell}}}(f)\right| e^{j\phi_{iR\vec{\ell}}(f)} \tag{28}$$

where

$$\phi_{i\,R\vec{\ell}}(f) = \frac{D_{i\,R\vec{\ell}}f}{\overline{U}} \tag{29}$$

with $D_{iR\vec{\ell}}$ representing the longitudinal separation between the point i on the rotor plane and the distance R along the LIDAR beam.

A. Components of Measurement Coherence

There are several factors that may cause a decrease in measurement coherence defined by equation 12. In addition to wind evolution, error sources characteristic of LIDAR measurements in non-evolving wind fields such as range weighting and directional bias will cause a loss of coherence. Figure 8 compares the components of coherence for three different measurement geometries by showing measurement coherence with various combinations of the error sources included. Each scenario involves a LIDAR located at the hub measuring wind at a radial distance of $r = 47.25$ m at an azimuth angle of $\psi = 90°$, but with different preview distances ($D = 24$, 58, and 130 meters). The curves in Fig. 8 do not include the effects of uv correlation in order to highlight the other sources of coherence loss. When $D = 24$ m, the measurement angle is large, longitudinal coherence (dashed) is relatively high, and the effects of range weighting are insignificant due to the short focal distance. Here, directional bias dominates the overall coherence, with wind evolution causing some degradation at higher frequencies. When $D = 130$ m, the measurement angle is low, longitudinal coherence is low due to wind evolution, and range weighting is significant due to the long focal distance. Wind evolution is the dominant component of measurement coherence, with range weighting adding a further loss of coherence. For the $D = 58$ m scenario, all three sources of coherence loss are significant. Directional bias and wind evolution both have very strong impacts, with range weighting causing an additional loss of coherence.

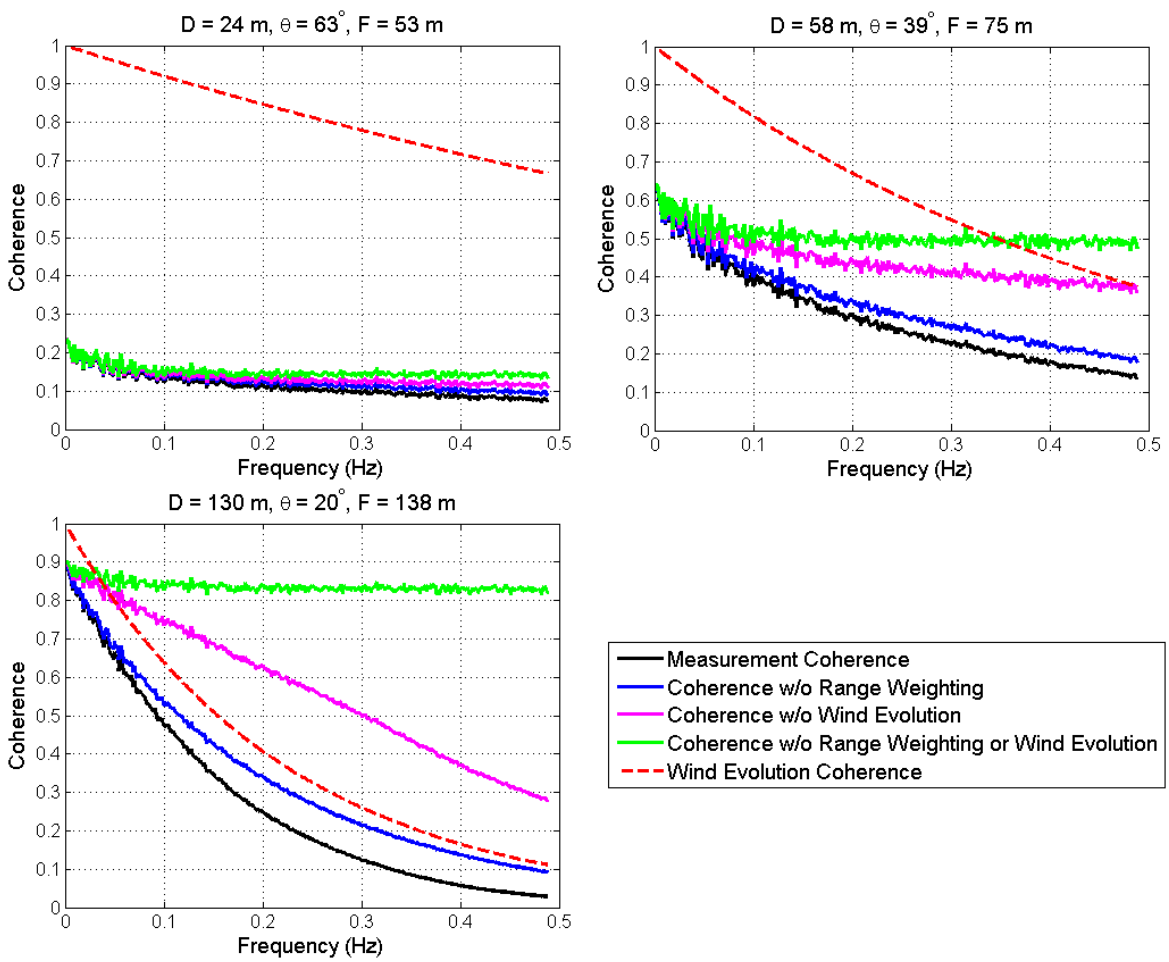

Figure 8. A comparison of the components of measurement coherence for a scanning LIDAR scenario with $r = 47.25$ m using the Great Plains-Low Level Jet wind field and exponential coherence with $\alpha = 0.45$.

Figure 8 reveals that the (green) coherence curves from directional bias alone are relatively constant over all frequencies and increase as measurement angle decreases. When the effects of uv and uw coherence are included, then measurement coherence due to directional bias changes because of the non-zero correlation between the u and v as well as u and w components. This behavior can be explained through equations

21 and 27. By comparing the green and magenta curves in Fig. 8, it can be seen that range weighting adds a significant coherence loss when wind evolution is not included, especially for larger preview distances. However, by comparing the blue and black curves, it is clear that with wind evolution included, range weighting never dominates the overall coherence loss.

VI. LIDAR Measurements of Evolving Wind Fields

Using the Great Plains-Low Level Jet wind field with the exponential coherence model for an unstable boundary layer, LIDAR measurement quality is assessed for realistic scanning geometries. Similar to the results for scanning LIDAR performance in frozen wind fields discussed in Section II-C, measurement quality is examined for different scan radii as a function of preview distance. However, instead of using RMS error to judge measurement quality, here the metrics are based on coherence between the measured wind and the wind that reaches the rotor, as described in equation 12, using the calculations outlined in Section V. Two metrics are used to reveal the measurement quality for different scan geometries. The first metric is the "coherence bandwidth," defined here as the bandwidth where the measurement coherence remains above 0.5. A higher coherence bandwidth yields a better measurement because more of the measured turbulence spectrum can be used in a wind preview-based controller. The second metric is the integral of measurement coherence, or the area under the coherence curve. The integration is only performed for a bandwidth of 0.5 Hz because the energy in the wind is relatively low for higher frequencies. A larger area under the coherence curve will yield a better measurement. Results based on the two metrics are similar, but both are provided here for comparison.

The following results compare measurement quality for different scan geometries and reveal the optimal preview distances in terms of maximizing the coherence bandwidth or coherence integral. For the exponential wind evolution model, the decay parameter a is varied to show the impact that wind evolution intensity has on optimal preview distance. Separate results are provided for four different LIDAR azimuth angles ψ. Using the definition of azimuth angle in Fig. 2, results are provided for $\psi = 90°$ and $-90°$, where the LIDAR is only measuring wind in the xy plane, $\psi = 0°$, where the LIDAR is measuring wind in the xz plane above hub height, and $\psi = 180°$, where wind is measured in the xz plane below hub height. These four azimuth angles were chosen because the wind spectra and transverse coherences are different in the y and z directions. In addition, ℓ_y will be positive for $\psi = 90°$ and negative for $\psi = -90°$. Similarly, ℓ_z will be positive for $\psi = 0°$ and negative for $\psi = 180°$. This allows us to investigate the impact of uv and uw cross-correlations in equations 21 and 27 for both positive and negative ℓ_y and ℓ_z components. Furthermore, the spectra and transverse coherence curves vary with height, so measurements above and below hub height are analyzed.

The chosen scan geometries are based on the NREL 5-MW turbine model. Scan radii of 15.75 m, 31.5 m, 47.25 m, and 63 m are investigated, which correspond to 25%, 50%, 75%, and 100% blade span. For the NREL 5-MW model, the LIDAR is located in the spinner of the turbine at a height of 90 meters.

For the four scan radii investigated, Fig. 9 compares the $\gamma^2 = 0.5$ coherence bandwidths of measurement coherence as a function of preview distance for a range of decay parameters. Note that the green curves represent a decay parameter $a = 0$, which is equivalent to no wind evolution (Taylor's frozen turbulence hypothesis). Coherence bandwidth curves are provided for the four different azimuth angles. For shorter scan radii, the preview distances that provide maximum coherence bandwidth are shorter because the degradation due to directional bias that enters the coherence calculations through equation 22 is lower than for larger scan radii. Therefore with small scan radii, the dominant source of coherence loss transitions from directional bias to wind evolution or range weighting at shorter preview distances.

In Fig. 9, the curves for azimuth angles $\psi = 90°$ and $\psi = 180°$ are very similar as are the curves for azimuth angles $\psi = 0°$ and $\psi = -90°$. For $\psi = 90°$ and $\psi = 180°$, the CPSDs between the u and v as well as the u and w components introduce a negative contribution in equations 21 and 27. This behavior is due to ℓ_y and $S_{uv}(f)$ both having positive signs and ℓ_z and $S_{uw}(f)$ both having negative signs. The negative contribution of the v and w components causes a reduction in both the magnitude of the measured LIDAR signal and the overall measurement coherence. In contrast, for $\psi = -90°$ and $\psi = 0°$, ℓ_y is negative while the sign of $S_{uv}(f)$ is positive and ℓ_z is positive while the sign of $S_{uw}(f)$ is negative. Therefore the CPSDs between the u and v as well as the u and w components introduce a positive contribution in equations 21 and 27. The positive contribution of the v and w components causes an increase in both the magnitude of the measured LIDAR signal and the overall measurement coherence.

Further variations between the curves for different azimuth angles in Fig. 9 reveal how the relative

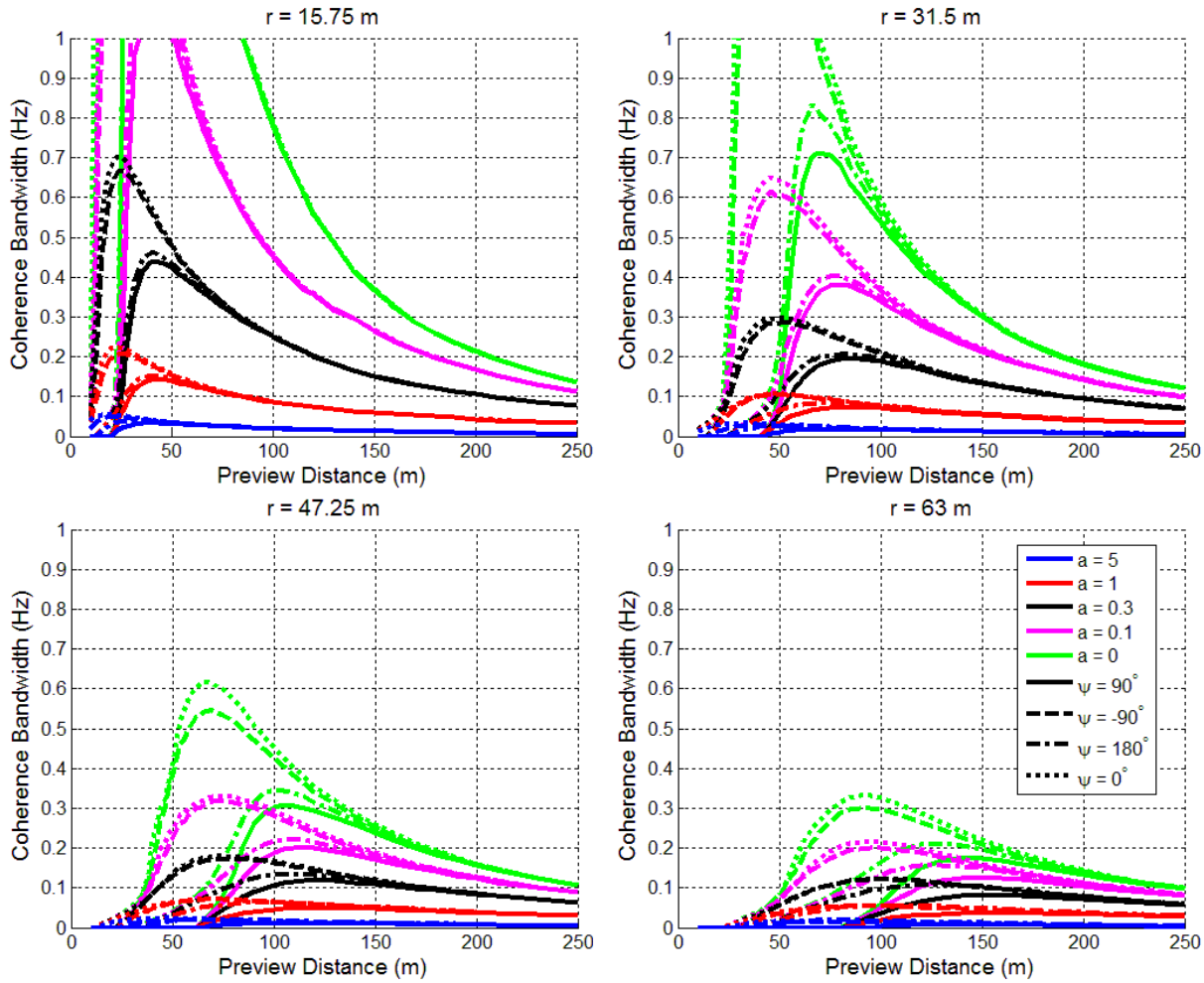

Figure 9. $\gamma^2 = 0.5$ coherence bandwidth vs. preview distance for the Great Plains-Low Level Jet wind field for scan radii of $r = 15.75$ m, 31.5 m, 47.25 m, and 63 m. Wind evolution is based on an exponential coherence model with various decay parameters.

magnitudes of the wind spectra components affect measurement coherence. Measurements at azimuth angles of $\psi = 0°$ and $\psi = 180°$ in the xz plane produce higher coherence bandwidths than measurements at $\psi = -90°$ and $\psi = 90°$ in the xy plane, respectively. The improved results for the measurements in the xz plane can be explained by examining the wind spectra in Fig. 6. The ratio between the v component of the wind spectrum to the u component is greater than the ratio between the w and u components at all heights, so the v component of the wind corrupts measurements more than the w component. Therefore, when measurements are confined to the xy plane, there is more coherence loss due to directional bias effects than when measurements are confined to the xz plane.

Figure 10 shows results for the same measurement scenarios as in Fig. 9, but with the integral of the coherence curves as the measurement quality metric. Most of the trends are similar to those in Fig. 9, but with slightly different optimal preview distances.

While the maximum coherence bandwidths are much lower for larger decay parameters as can be expected, interestingly, the optimal measurement preview distances do not change very much as a is varied when using the coherence bandwidth metric. When using the integral of coherence as a metric, the optimal preview distance is much more sensitive to changes in the decay parameter. Figures 11 and 12 show the optimal preview distance as a function of decay parameter for the four azimuth angles at the four scan radii when the quality metrics are the coherence bandwidth and the integral of the coherence curve, respectively. Also shown in these plots are the maximum bandwidths and integrals achieved at the optimal preview distances. Instead of decreasing monotonically as the wind evolution intensity increases, as might be expected, the

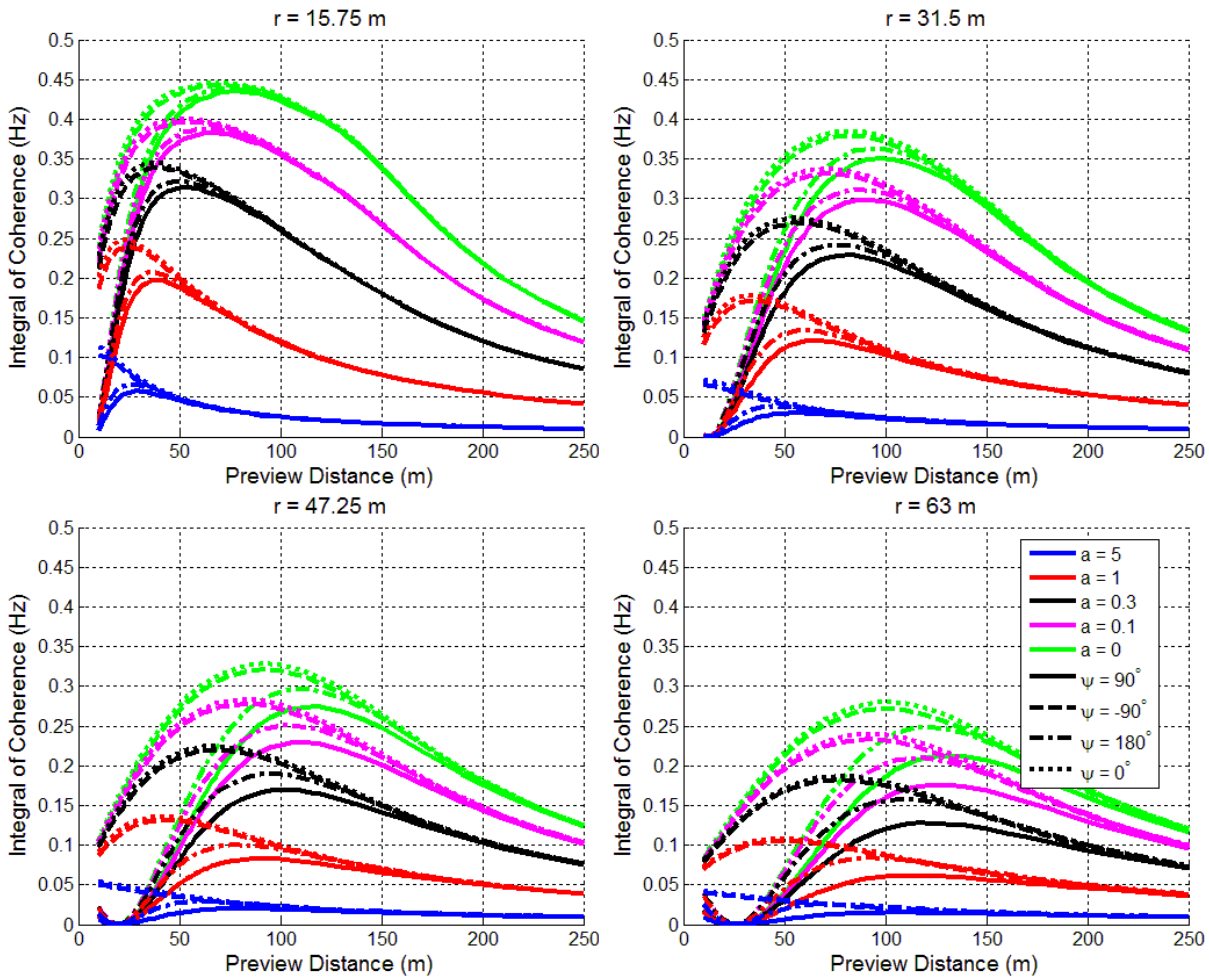

Figure 10. Integral of measurement coherence from 0 Hz to 0.5 Hz vs. preview distance for the Great Plains-Low Level Jet wind field for scan radii of r = 15.75 m, 31.5 m, 47.25 m, and 63 m. Wind evolution is based on an exponential coherence model with various decay parameters.

optimal preview distances based on coherence bandwidth become greater as the decay parameter is increased up until a certain point where they begin to decrease. For both metrics, there is a considerable difference between the optimal preview distances for the different azimuth angles. This suggests that when measurement coherence is higher due to positive contributions from the uv and uw cross-correlations or weaker transverse wind components, the optimal preview distance is shorter because the directional bias effects are less severe.

VII. Conclusions and Future Work

In this paper, we have explained how wind evolution can be described by longitudinal coherence functions in a wind field. We examined the coherence between LIDAR measurements and true wind speeds in evolving wind fields for realistic preview measurement scenarios. Wind evolution was introduced to a frozen wind field that is characteristic of the U.S. Great Plains, using a simple exponential model of longitudinal coherence that is a function of the non-dimensional value kD. Using wind spectra and coherence functions determined from the Great Plains-Low Level Jet wind field, we calculated measurement coherence directly, without having to perform computationally expensive and memory intensive simulations of LIDAR measurements in evolving wind fields.

Measurement coherence loss is dominated by the directional bias source of error for short preview distances due to high measurement angles. Further, the coherence is sensitive to both the cross-correlation of the wind components as well as the relative magnitudes of the transverse and longitudinal components of wind speed.

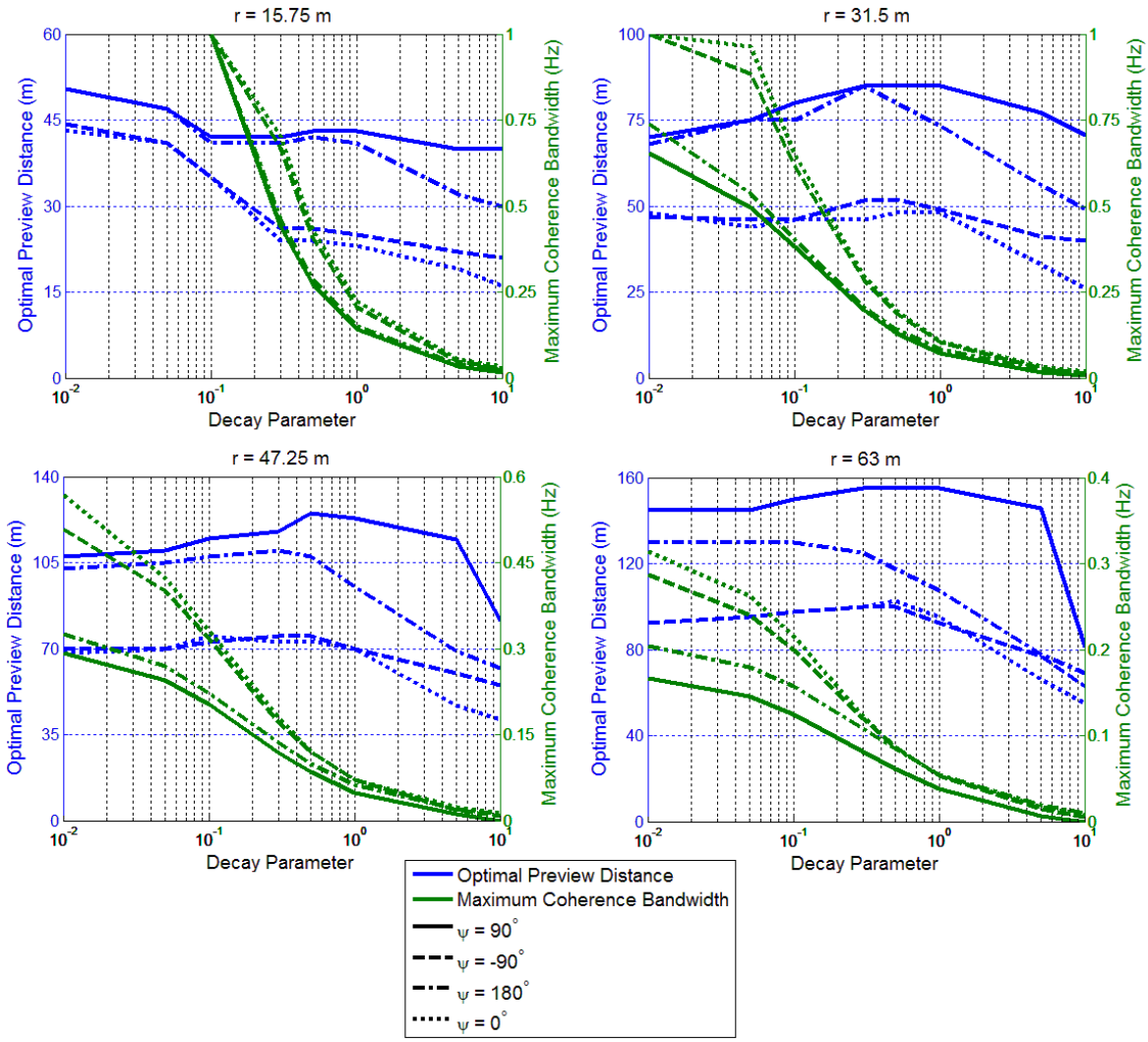

Figure 11. Maximum $\gamma^2 = 0.5$ coherence bandwidth preview distance vs. decay parameter for the Great Plains-Low Level Jet wind field using the exponential wind evolution model for scan radii of $r = 15.75$ m, 31.5 m, 47.25 m, and 63 m. Corresponding maximum coherence bandwidths are shown using a secondary axis (right) in green.

As preview distance increases, the main source of coherence loss transitions to wind evolution. Figure 8 shows how LIDAR range weighting is not the dominant source of coherence loss when wind evolution is introduced, but can have a significant impact when the the intensity of wind evolution is low and the preview distance is large.

Varying the intensity of wind evolution by adjusting the decay parameter affects the measurement coherence considerably. However, using coherence bandwidth as a metric, it was revealed that for a given scan radius the optimal preview distance is not very sensitive to the amount of wind evolution. When using the area under the coherence curve as a metric, the optimal preview distance for a given scan radius is more sensitive to changes in the decay parameter.

Based on the results from Section VI, optimal preview distances for LIDAR measurements in evolving wind fields based on coherence bandwidth are roughly 60 meters for a scan radius of $r = 31.5$ meters, 80 meters for $r = 47.25$ meters, and 120 meters for $r = 63$ meters for decay parameters less than 1. Using the integral of coherence as a metric, the optimal preview distances vary considerably as the decay parameter changes. Optimal preview distances using RMS error as the metric in a frozen wind field (Fig. 4) are around 115 meters, 150 meters, and 225 meters for scan radii of $r = 31.5$ m, $r = 47.25$ m, and $r = 63$ m, respectively. While the exact preview distances vary depending on the metric used, with wind evolution

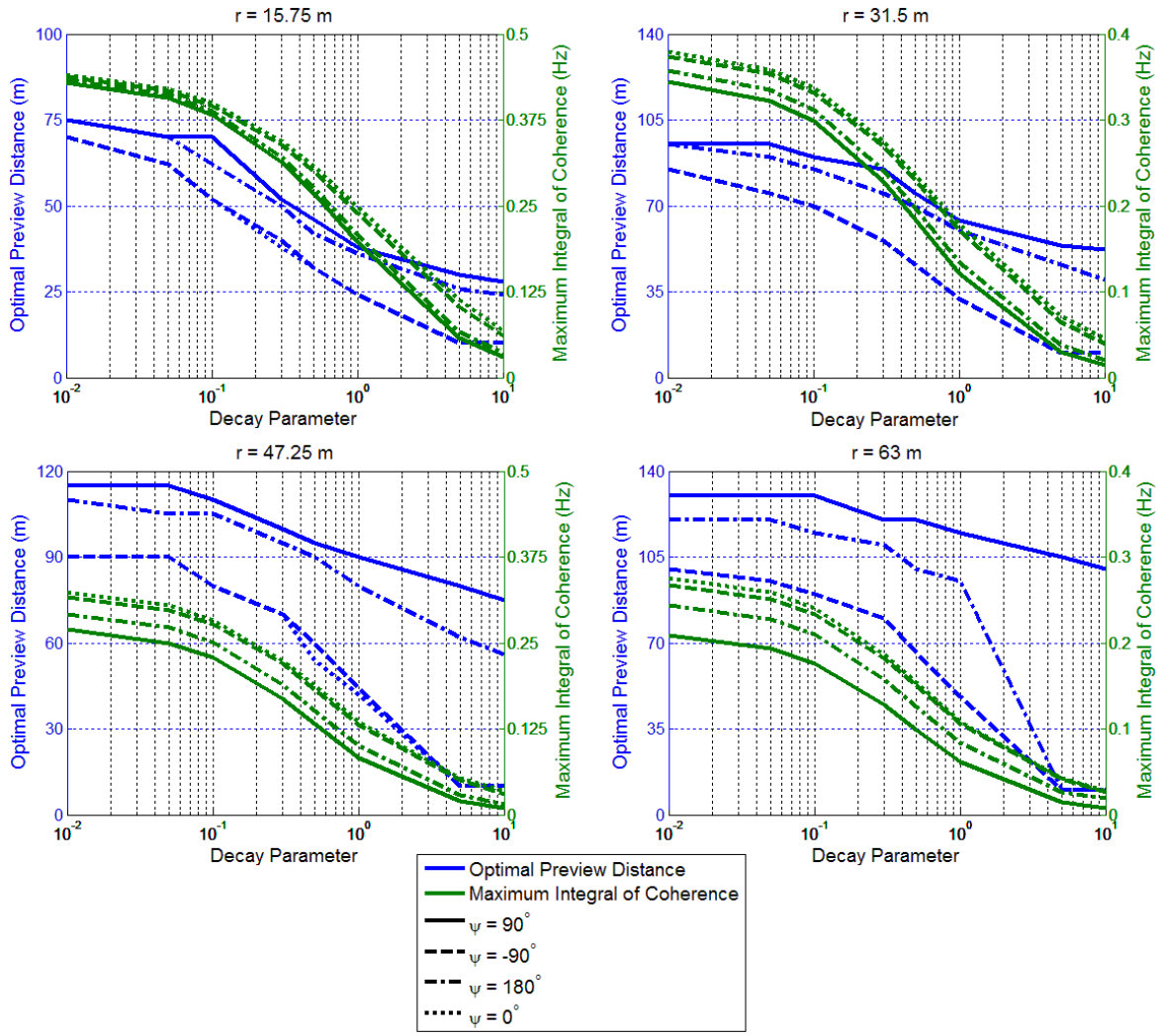

Figure 12. Optimal preview distance based on integral of measurement coherence vs. decay parameter for the Great Plains-Low Level Jet wind field using the exponential wind evolution model for scan radii of $r = 15.75$ m, 31.5 m, 47.25 m, and 63 m. Corresponding maximum integrals of measurement coherence from 0 Hz to 0.5 Hz are shown using a secondary axis (right) in green.

introduced, optimal preview distances based on coherence bandwidth are roughly half of those in frozen wind fields based on RMS error. However, when comparing results based on coherence bandwidth for different decay parameters, it can be seen that unless the intensity of evolution is very strong, the optimal preview distances are almost the same with wind evolution or without (when the decay parameter $a = 0$).

Future work will include studying large eddy simulations of the boundary layer to determine more realistic longitudinal coherence functions. In addition, by examining LES wind fields, more accurate coherence functions can be calculated for points in a wind field that are separated in both the longitudinal and transverse directions. Using these coherence functions, it will no longer have to be assumed that the coherence between two arbitrary points in a wind field is the product of longitudinal and transverse coherence.

Although not discussed in this paper, an additional source of error in wind speed measurements is the effect of the induction zone upwind of the rotor. The induction zone, which extends roughly one rotor diameter in front of the turbine, has the effect of slowing down the advection velocity of the wind near the rotor as well as distorting the turbulence. The impact of the induction zone on wind speed measurements is an area of future study.

Acknowledgments

The authors wish to thank Alan Wright, Fiona Dunne, and Jason Laks for discussions on desired characteristics of wind speed measurement devices that can enable preview-based control methods for wind turbines and Ned Patton from the National Center for Atmospheric Research for providing LES wind fields.

References

[1] J. Laks, L. Pao, A. Wright, N. Kelley, and B. Jonkman, "The use of preview wind measurements for blade pitch control," *IFAC J. Mechatronics*, vol. 21, no. 4, pp. 668–681, Jun. 2011.

[2] F. Dunne, L. Y. Pao, A. D. Wright, B. Jonkman, and N. Kelley, "Adding feedforward blade pitch control to standard feedback controllers for load mitigation in wind turbines," *IFAC J. Mechatronics*, vol. 21, no. 4, pp. 682–690, Jun. 2011.

[3] D. Schlipf and M. Kühn, "Prospects of a collective pitch control by means of predictive disturbance compensation assisted by wind speed measurements," in *Proc. German Wind Energy Conference (DEWEK)*, Bremen, Germany, Nov. 2008.

[4] D. Schlipf, D. Trabucchi, O. Bischoff, M. Hofsäß, J. Mann, T. Mikkelsen, A. Rettenmeier, J. Trujillo, and M. Kühn, "Testing of frozen turbulence hypothesis for wind turbine applications with a scanning lidar system," in *Proc. International Symposium for the Advancement of Boundary Layer Remote Sensing*, Paris, France, Jun. 2010.

[5] J. Laks, L. Pao, E. Simley, A. Wright, N. Kelley, and B. Jonkman, "Model predictive control using preview measurements from lidar," in *Proc. 49th AIAA Aerospace Sciences Meeting*, Orlando, FL, Jan. 2011.

[6] F. Dunne, L. Y. Pao, A. D. Wright, B. Jonkman, N. Kelley, and E. Simley, "Adding feedforward blade pitch control for load mitigation in wind turbines: Non-causal series expansion, preview control, and optimized FIR filter methods," in *Proc. 49th AIAA Aerospace Sciences Meeting*, Orlando, FL, Jan. 2011.

[7] E. Simley, L. Pao, R. Frehlich, B. Jonkman, and N. Kelley, "Analysis of wind speed measurements using coherent lidar for wind preview control," in *Proc. 49th AIAA/ASME Wind Energy Symposium*, Orlando, FL, Jan. 2011.

[8] D. Medici, S. Ivanell, J.-A. Dahlberg, and P. Alfredsson, "The upstream flow of a wind turbine: blockage effect," *Wind Energy*, vol. 14, pp. 691–697, 2011.

[9] B. Jonkman, "TurbSim user's guide: Version 1.50," National Renewable Energy Laboratory, NREL/TP-500-46198, Golden, CO, Tech. Rep., 2009.

[10] J. Jonkman, S. Butterfield, W. Musial, and G. Scott, "Definition of a 5-MW reference wind turbine for offshore system development," National Renewable Energy Laboratory, NREL/TP-500-38060, Golden, CO, Tech. Rep., 2009.

[11] R. Frehlich and M. Kavaya, "Coherent laser performance for general atmospheric refractive turbulence," *Applied Optics*, vol. 30, no. 36, pp. 5325–5352, Dec. 1991.

[12] M. Courtney, R. Wagner, and P. Lindelöw, "Commercial lidar profilers for wind energy. a comparative guide," in *Proc. European Wind Energy Conference*, Brussels, Belgium, Apr. 2008.

[13] T. Mikkelsen, K. Hansen, N. Angelou, M. Sjöholm, M. Harris, P. Hadley, R. Scullion, G. Ellis, and G. Vives, "Lidar wind speed measurements from a rotating spinner," in *Proc. European Wind Energy Conference*, Warsaw, Poland, Apr. 2010.

[14] F. Dunne, L. Pao, A. Wright, B. Jonkman, and N. Kelley, "Combining standard feedback controllers with feedforward blade pitch control for load mitigation in wind turbines," in *Proc. 48th AIAA Aerospace Sciences Meeting*, Orlando, FL, AIAA-2010-250, Jan. 2010.

[15] R. A. Pielke and H. A. Panofsky, "Turbulence characteristics along several towers," *Boundary-Layer Meteorology*, vol. 1, no. 2, pp. 115–130, 1970.

[16] D. Schlipf, "Wind turbine control using lidar: Notes to presentation," in *PhD Summer School: Remote Sensing for Wind Energy*, Roskilde, Denmark, Jun. 2011.